ADVANCED MATERIALS
www.advmat.de

Multifunctional Fe_5C_2 Nanoparticles: A Targeted Theranostic Platform for Magnetic Resonance Imaging and Photoacoustic Tomography-Guided Photothermal Therapy

Jing Yu, Ce Yang, Jingdingsha Li, Yichen Ding, Lei Zhang, Muhammad Zubair Yousaf, Jian Lin, Rui Pang, Lanbin Wei, Lili Xu, Fugeng Sheng, Changhui Li, Gongjie Li, Lingyun Zhao,* and Yanglong Hou**

Over the past decade, cancer has been one of the most significant causes of mortality worldwide.[1] Fortunately, imaging diagnostic has been emerging a powerful technology in assisting cancer therapy in terms of early detection and targeting therapy. One of the key challenges in cancer therapy is to develop tumor-selective methods that do not damage normal cells. As a minimal invasive local cancer therapy, photothermal therapy (PTT) — a cancer-cell "burning" treatment that uses electromagnetic radiation, specifically near infrared (NIR) energy with the help of a "photo-absorbing agent" — has attracted intensive interests recently.[2] The materials applied for PTT usually hold strong optical absorbance in the NIR due to their surface plasmon resonance effects, for example, various gold-based nanostructures (gold nanorods (NRs), nanostars, nanocages, and gold shells).[3] However, the morphology of part of these nanostructures will change under long periods of irradiation, which will subsequently alter their optical properties and decrease NIR absorbance.[4] Therefore, alternative agents with strong NIR absorbance as well as high stability are greatly desirable. So far, carbon-based agents, such as fullerenes, carbon nanotubes, and graphene, are being considered as promising alternates owing to their distinctive physical and chemical properties.[5]

Generally, it would be critically important to understand the state of the agents after both in vivo administration and post-treatment. Therefore, imaging-guided therapy is highly desirable. Currently, photoacoustic tomography (PAT) and magnetic resonance imaging (MRI) have been widely applied to imaging diagnostics in oncology clinics. PAT can depict subsurface tissue structures, while MRI can offer higher resolution and deeper tissue penetration.[6] Therefore, it would be a wise protocol to integrate MRI and PAT into a single probe, which offers the possibility of combining the contrast-based volume imaging and edge detection, and realizes "self-confirming for fault-free diagnosis".[7] Such a multimodality probe, which integrates dual modal imaging with therapeutic PTT, can further achieve early diagnosis and therapy of cancer.[8]

In recent years, novel theranostic agents, which are usually fabricated of functional nanocomposites for multimodal imaging-guided therapy, have exhibited great application potential in medicine.[9] Under the guidance of PAT-MRI, the probes for PTT are usually allowed to serve as contrast agents for PAT by further transforming the resulted heat into ultrasound waves. In addition, with the aid of magnetic materials, hypointensities on T_2-weighted MRI maps can be induced for better contrast effect.[10] For instance, magnetic nanoparticle (NP)-anchored graphene nanosheets and iron oxide-conjugated gold NRs have been applied in MRI- and PAT-guided PTT.[11] However, these probes generally comprise multiple components, such as distinct magnetic and high-NIR-absorbance parts. Recently, Fe_3O_4@$Cu_{2-X}S$ core–shell NPs were also reported for dual modal imaging and PTT, in which all the functionalities were realized within one core–shell particle.[4a] However, this protocol still needs intricate and multi-step synthetic processes, and most of the above-mentioned probes mainly rely on the passive targeting effect (i.e., the enhanced permeability and retention (EPR) effect for tumor targeting). It is worth noting that some tumors will not exhibit EPR effect and, consequently, there are great demands to fabricate multifunctional probes via simple methods and achieve specific interaction with certain cancer cells.

Recently, we reported the synthesis of magnetic Hägg iron carbide NPs (Fe_5C_2 NPs) with a thin carbon shell coating by a one-pot synthetic method.[12] Note that Fe_5C_2 NPs possess

J. Yu, C. Yang, Dr. M. Z. Yousaf, Prof. Y. Hou
Department of Materials Science and Engineering
College of Engineering, Peking University, Beijing 100871, China
E-mail: hou@pku.edu.cn
J. Li, R. Pang, L. Wei, Prof. L. Zhao
Institute of Medical Physics
Key Laboratory of Particle & Radiation Imaging
Ministry of Education
Department of Engineering Physics
Tsinghua University
Beijing 100084, China
E-mail: nuszly@gmail.com
Y. Ding, Prof. C. Li
Department of Biomedical Engineering
College of Engineering, Peking University
Beijing 100871, China
L. Zhang, L. Xu, Dr. F. Sheng, G. Li
Department of Radiology
Affiliated Hospital of the Academy of Military Medical Sciences
Beijing 100071, China
E-mail: shengfugeng@gmail.com
Prof. J. Lin
Synthetic and Functional Biomolecules Center
Department of Chemical Biology
College of Chemistry and Molecular Engineering
Peking University
Beijing 100871, China

DOI: 10.1002/adma.201305811

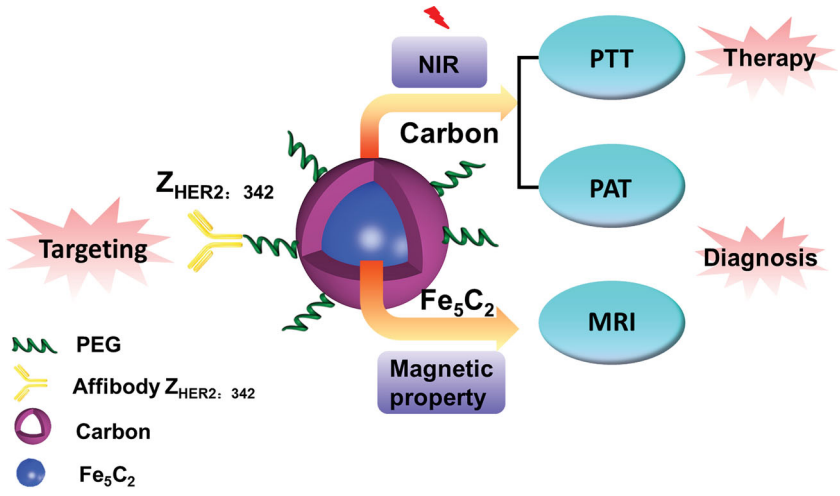

Scheme 1. Schematic illustration for the design of Fe_5C_2 NPs as a targeted theranostic platform.

magnetic features and a carbon-coated structure; they therefore provide a unique opportunity to develop multifunctional probes with MRI, PTT, and PAT for imaging-guided therapy. Herein, an Fe_5C_2-based probe is designed by modifying Fe_5C_2 NPs with 1,2-distearoyl-*sn*-glycero-3-phosphoethanolamine-*N*-[amino(polyethylene glycol)-2000] (DSPE-PEG-NH_2) and a new class of affinity proteins ($Z_{HER2:342}$) that can selectively bind to the extracellular domain of HER2 for ovarian-cancer targeting.[13] The Fe_5C_2-based probe (Fe_5C_2-$Z_{HER2:342}$) mainly possesses the following advantages (**Scheme 1**): i) the high-saturation-magnetization nature of the Fe_5C_2 core makes the NPs an excellent candidate for T_2 MRI contrast agents; ii) the carbon on the surface endows the NPs with high absorption in NIR for PTT and PAT, and also protects the Fe_5C_2 core from oxidation, thus offering good stability of the agents; and iii) conjugation of the affibody makes tumor-only targeting theranostics feasible. The Fe_5C_2-$Z_{HER2:342}$ probe exhibited enhanced hypo-intensities in MRI in comparison to Resovist, and induced a stronger photoacoustic signal and photothermal effect than gold NRs. In vitro study indicates that the probe could selectively combine with HER2 overexpressed cells, and effectively induce morbidity in the cell after exposure under NIR light. Long-lasting negative-contrast enhanced MRI as well as high PAT signals were observed at the tumor site in ovarian-tumor-bearing mice by i.v. injection. Under the guidance of imaging, the tumor was obviously ablated by PTT after NIR irritation. More importantly, almost no systematic side effects were observed during the treatment through the evaluation of the loss of body weight, and morphological and pathological examinations. To the best of our knowledge, Fe_5C_2-based NPs have not yet been explored as multifunctional platforms in imaging-guided therapy, and Fe_5C_2-$Z_{HER2:342}$ is of great promise as a multifunctional probe for cancer theranostic applications.

Transmission electron microscopy (TEM) showed that the Fe_5C_2 NPs has a core–shell structure with an overall diameter of about 20 nm, which was further confirmed by dynamic light scattering (DLS) (**Figure 1**a and Figure S1, in the Supporting Information). As revealed from high-resolution TEM (HRTEM) and X-ray photoelectron spectroscopy (XPS) (Figure S2 and S3, Supporting Information), the shell structure was a layer of amorphous carbon,[12] while the core part showed highly crystalline features with a lattice spacing of 0.205 nm, which corresponds to the (510) plane of Fe_5C_2. X-ray powder diffraction (XRD) analysis confirmed the chemical structure of Fe_5C_2 (JCPDS no. 36–1248; Figure S4, Supporting Information). To endow a hydrophilic nature as well as long-circulation property to Fe_5C_2 NPs, DSPE-PEG-NH_2 was applied to form Fe_5C_2-PEG NPs; the coating amount for DSPE-PEG-NH_2 was 11.41% (Figure S5, Supporting Information). Both the morphology and the size of the Fe_5C_2-PEG NPs were well maintained; the core part remains Fe_5C_2, and the hydrodynamic diameter was measured to be 50 nm (Figure S1, S4, and S6, Supporting Information), demonstrating the stability of the Fe_5C_2-PEG NPs.

Magnetization measurements showed that Fe_5C_2 NPs possessed super-paramagnetic feature with a saturation magnetization (Ms) of 125 emu g^{-1} at room temperature, no Ms value loss was observed after PEGylation (Figure 1b). After storing in aqueous dispersion for 6 months, only a slight decrease of Ms value was observed (112 emu g^{-1}), which is still higher than that of iron oxide (ca. 80 emu g^{-1});[14] this can probably be ascribed to the protection by the carbon shell. The T_2-weighted MRI of Fe_5C_2 NPs were taken on a 3 T clinic MRI scanner. As shown in Figure 1c, the signal intensity decreased with the increase of iron concentration. Compared with Resovist, a commercially available T_2-weighted MRI contrast agent consisting of Fe_3O_4 NPs with comparable hydrodynamic diameters of 60 nm,[15] Fe_5C_2 NPs can induce stronger hypo-intensities due to its higher magnetization.[16] Transverse relaxivity (r_2) is further calculated, which shows 312 mM^{-1} s^{-1} for Fe_5C_2 NPs, higher than that of Resovist (174 mM^{-1} s^{-1}) (Figure 1d).

Considering the potential applications of Fe_5C_2 NPs with a thin carbon coating in PTT and PAT, ultraviolet–visible–NIR optical absorption spectra of aqueous suspensions were examined. The NPs exhibited an appreciable absorbance in the NIR region, which locates at the tissue transparency window (Figure S7, Supporting Information). Taking the absorption at 808 nm, for example, the corresponding metal-atom (Fe) molar extinction coefficient was calculated to be 3672 cm^{-1} M^{-1} (Figure S8, Supporting Information). The high NIR absorbance of Fe_5C_2 NPs suggested that it would be an excellent photoabsorbing agent for potential PTT and PAT.

Under NIR laser radiation (λ = 808 nm, 2 W cm^{-2}), Fe_5C_2 NPs exhibited significant temperature increment, which is even greater than that of gold NRs (aspect ratio of 3.5) and Resovist (Figure 1e).[17] The decrease of either the concentration of Fe_5C_2 NPs or laser intensity will slow down the temperature increment, illustrating that the thermal energy was converted by the NIR optical absorbance of Fe_5C_2 NPs (Figure S9, Supporting Information). The photothermal stability of Fe_5C_2 NPs and gold NRs were investigated by TEM characterization, which clearly demonstrated that Fe_5C_2 NPs are more stable during NIR irradiation, i.e., the morphology of Fe_5C_2 NPs maintained integrity, while a significant alteration was observed for gold

Adv. Mater. **2014**,
DOI: 10.1002/adma.201305811

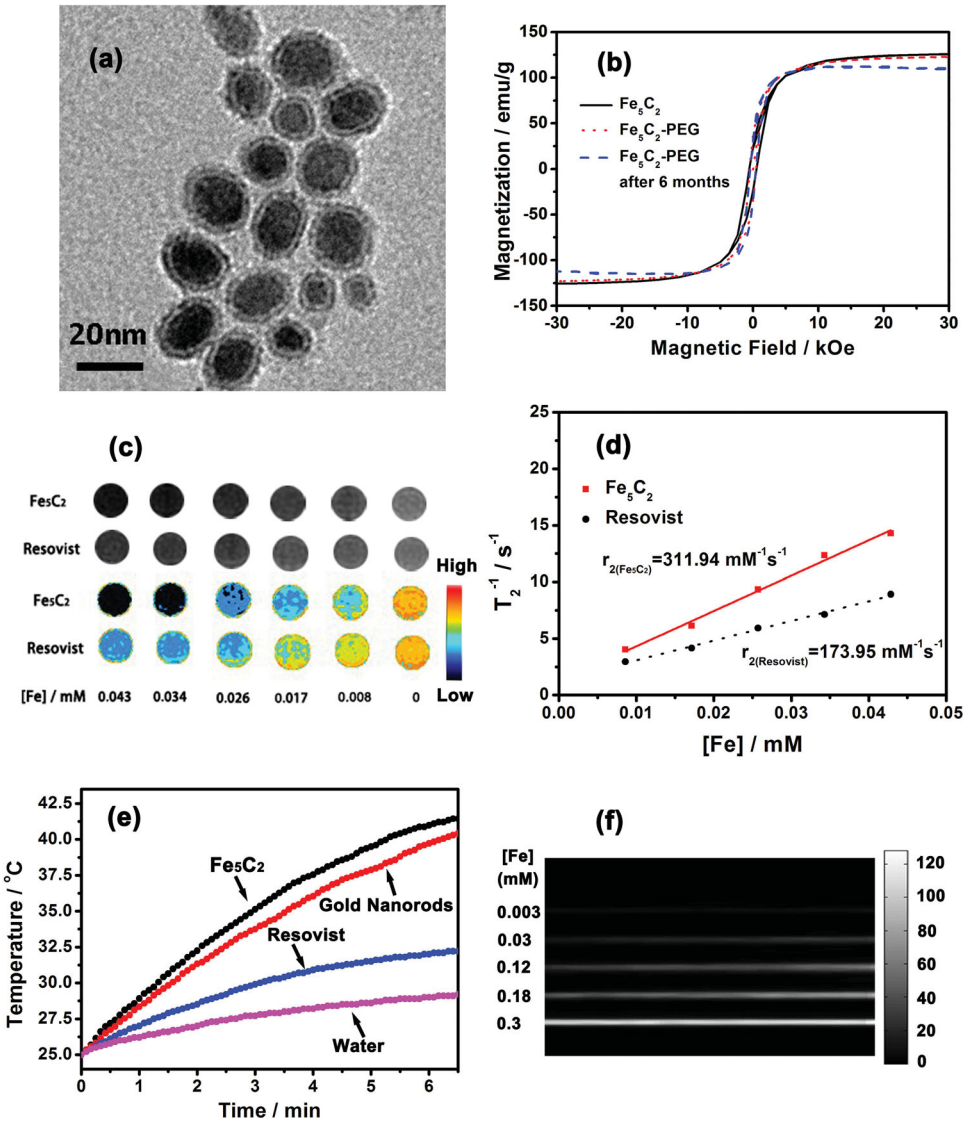

Figure 1. a) TEM image of as-synthesized Fe_5C_2 NPs. b) Room-temperature magnetic hysteresis loops of Fe_5C_2 NPs before (black line) and after (red line) modification. The blue line is the room-temperature magnetic hysteresis loops for Fe_5C_2 NPs after modification and exposed in water for 6 months. c) T_2-weighted MR images of Fe_5C_2 NPs (upper) and Resovist (down) at various concentrations of iron at 3 T. The lower two rows are their corresponding pseudo-color images. d) T_2 relaxation rate ($1/T_2$) as a function of Fe concentrations for the Fe_5C_2 NPs and Resovist. e) Temperature-evolution curves for aqueous dispersions of pure water and Fe_5C_2 NPs/Resovist/gold nanorods at the same concentration (0.5 mM Fe or Au) under continuous radiation of an 808 nm NIR laser at 2 W cm^{-2}. f) PAT images of Fe_5C_2 NPs with different concentrations.

NRs (Figure S10, Supporting Information). Photoacoustic signals from Fe_5C_2 NPs was then detected on a home-made PAT system.[18] A bright signal can be observed with the increase of the concentration of Fe_5C_2 NPs (Figure 1f). Compared with gold NRs (aspect ratio of 3.5), Fe_5C_2 NPs can induce higher signal intensity (Figure S11, Supporting Information).

The HER2 receptor is found to be associated with homo- or hetero-dimerization by clustering on the plasma membrane of some specific cell lines. When $Z_{HER2:342}$-conjugated NPs bind to HER2 receptors, the receptor clustering is expected to induce the aggregation of a large amount of NPs with the cells. The targeting specificity of Fe_5C_2-$Z_{HER2:342}$ NPs to HER2-positive SK-OV-3 cells was assessed by T_2-weighted MRI. It presented an enhanced darkening compared to Fe_5C_2-PEG NPs, suggesting a much higher level of cellular uptake due to the $Z_{HER2:342}$ conjugation (**Figure 2**a). The potential toxicity of Fe_5C_2-$Z_{HER2:342}$ NPs on macrophages (RAW 264.7), HER2-positive cells (SK-BR-3 and SK-OV-3 cells), and HER2-negative cells (NIH 3T3 and HeLa cells) were tested.[19] As shown in Figure 2b, no significant cytotoxicity was observed within all cell lines under our investigated concentrations.

We subsequently examined cell viability after exposure to 808 nm laser (2 W cm^{-2} for 3 min) on SK-OV-3 cells by MTT assays. As predicted, a laser-induced therapeutic effect mediated by Fe_5C_2-$Z_{HER2:342}$ NPs was more significant compared to that by Fe_5C_2-PEG NPs. Additionally, there was almost no cytotoxicity observed in Fe_5C_2-$Z_{HER2:342}$ alone or the laser group (Figure 2c). By staining with Calcein-AM and PI, the photothermal effect

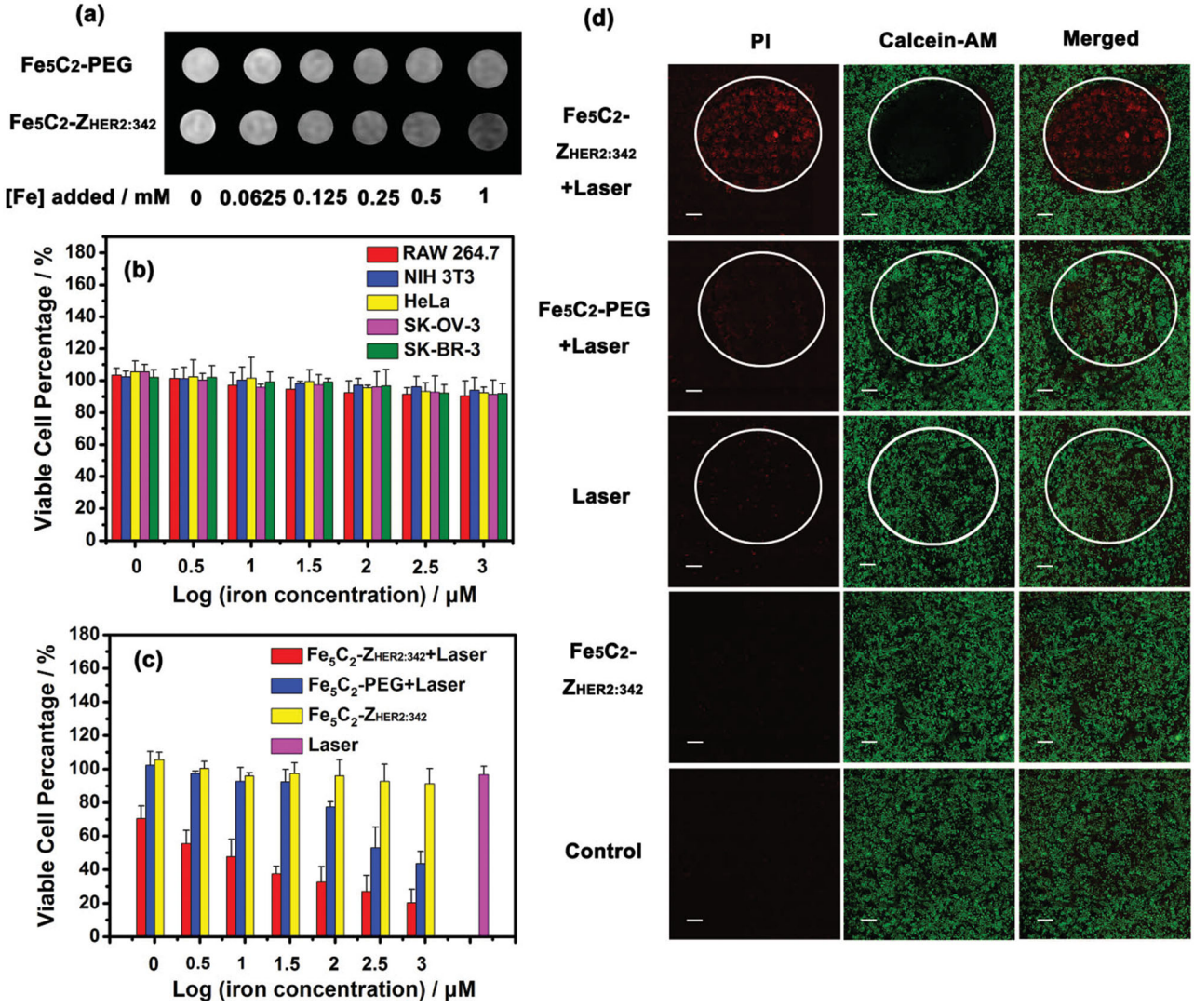

Figure 2. a) T_2-weighted MR images of Fe_5C_2-$Z_{HER2:342}$ NPs and Fe_5C_2 NPs treated with SK-OV-3 cells. b) MTT assays of Fe_5C_2-$Z_{HER2:342}$ NPs on RAW 264.7 cells, NIH 3T3 cells, SK-BR-3 cells, SK-OV-3 cells, and HeLa cells in tested concentration range (1–1000 μM Fe). c) MTT assays on SK-OV-3 cells with Fe_5C_2-$Z_{HER2:342}$ or Fe_5C_2-PEG with or without NIR irradiation. d) Fluorescence microscopy image of (left) necrotic or apoptotic cells, stained with PI; (middle) live cell, stained with Calcein-AM, and (right) merged image of SK-OV-3 cells incubated with Fe_5C_2-$Z_{HER2:342}$, and irradiated with NIR; SK-OV-3 cells incubated with Fe_5C_2-PEG, and irradiated with NIR; SK-OV-3 cells irradiated with NIR only; SK-OV-3 cells incubated with Fe_5C_2-$Z_{HER2:342}$ only; and SK-OV-3 cells without any treating, respectively (from top to bottom). Scale bars: 600 μm. In all the NIR irradiation experiments, irradiation was at a power density of 2 W cm^{-2} for 3 min within the white circle.

was further investigated by distinguishing the apoptotic cells with living cells. Compared with the control group, severe cell death was observed when treated with Fe_5C_2-$Z_{HER2:342}$ NPs along with laser irradiation (Figure 2d). However, cells incubated with Fe_5C_2-PEG NPs only underwent slightly apoptosis after exposure to laser. This effect was not observed in cells exposed to laser only or cells incubated with Fe_5C_2-$Z_{HER2:342}$ without irritation, which is in agreement with the MTT results.

Inspired by the promising in vitro data, we then utilized Fe_5C_2 NPs as a multifunctional platform for in vivo tumor-selective imaging. All the experiments involving animals were performed according to the guidelines approved by the Institutional Animal Care and Use Committee (IACUC) of Tsinghua University. T_2-weighted MR images were taken before and after intravenous injection of Fe_5C_2-$Z_{HER2:342}$ or Fe_5C_2-PEG on female Balb/c mice bearing an SK-OV-3 tumor. Signal dropping at the tumor sites could be observed in both of groups, while the signal decreasing from the Fe_5C_2-$Z_{HER2:342}$-treated mice is more significant (**Figure 3**a,b). The relative signal intensity was also calculated (Figure S12, Supporting Information). In both of groups, the lowest signal comes 24 h post-injection, making it the optimal time for tumor theranostics. Interestingly, after 3 d, the MR signal from the Fe_5C_2-PEG treated mice begins to recover, while the Fe_5C_2-$Z_{HER2:342}$-treated group maintains the low signal, suggesting a longer retention of Fe_5C_2-$Z_{HER2:342}$ NPs at the tumor site. One mouse from each group was sacrificed 24 h or 7 d after injection for Prussian blue staining. More positively stained areas are observed in the Fe_5C_2-$Z_{HER2:342}$-treated

Adv. Mater. 2014,
DOI: 10.1002/adma.201305811

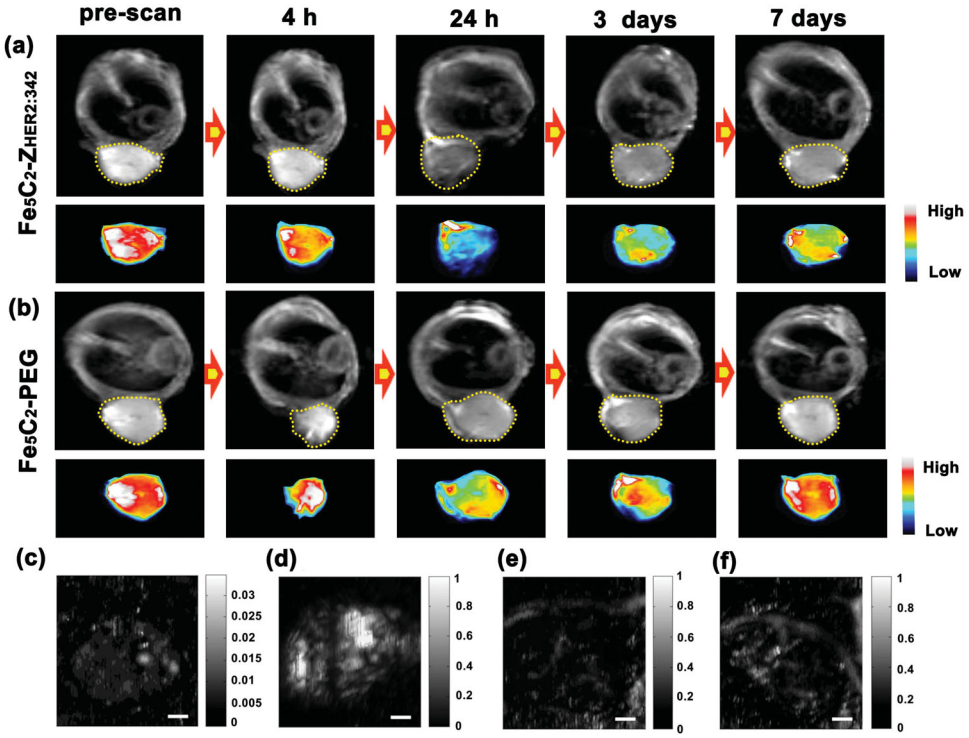

Figure 3. T_2-weighted MR images of SK-OV-3 tumor-bearing mice before and after intravenous injection of: a) Fe_5C_2-$Z_{HER2:342}$, and, b) Fe_5C_2-PEG for different time points. The tumor sites are in the right axillary region, and circled by a yellow dashed line. The lower row of each figure is the pseudo-color image for the tumor site. c–f) PAT results of tumor site: c,e) before, and, d,f) after intravenously injecting with: d) Fe_5C_2-$Z_{HER2:342}$, and, f) Fe_5C_2-PEG for 24 h. Scale bars are 1 mm. The tumor sites are at the right rear flank. Grey bars are photoacoustic signal intensity.

mouse than the mouse administrated with Fe_5C_2-PEG NPs. Even 7 d post-injection, the strong blue signals from the Fe_5C_2-$Z_{HER2:342}$-treated mouse still remain, while an indiscernible signal is observed in the Fe_5C_2-PEG injected mouse (Figure S13, Supporting Information). Sequentially, we investigated the in vivo PAT of Fe_5C_2 NPs (24 h post-injection) to confirm the targeted tumor accumulation by $Z_{HER2:342}$. Strongly enhanced photoacoustic signals in the tumors were observed after injection with Fe_5C_2-$Z_{HER2:342}$ NPs, while a much lower signal was emitted from the Fe_5C_2-PEG treated one, indicating that Fe_5C_2-$Z_{HER2:342}$ NPs can also be used as a PAT probe for targeted tumor imaging (Figure 3c–f).

Encouraged by the selective accumulation of Fe_5C_2-$Z_{HER2:342}$ NPs within tumor sites, we further carried out in vivo PTT under the guidance of imaging on ovarian-tumor-bearing mice. 30 mice were randomly divided into five groups (n = 6): 1) Fe_5C_2-$Z_{HER2:342}$ treated group with NIR irradiation; 2) Fe_5C_2-PEG treated group with NIR irradiation; 3) laser irradiation-only group; 4) Fe_5C_2-$Z_{HER2:342}$ treated-only group, and, 5) a control group with saline administration. After 24 h injection, when maximum NPs were accumulated into tumors, laser irradiation was performed at the tumor site for 3 min at a power of 2 W cm^{-2}. Within 2 min irradiation, the tumor center temperature of Fe_5C_2-$Z_{HER2:342}$-treated group can elevate to ca. 47 °C from ca. 26 °C, which is sufficient to ablate the tumors. However, only slight temperature increments (ΔT = 8 °C) were observed on the mice administrated with Fe_5C_2-PEG, and laser exposure-only induced negligible temperature increase (Figure S14, Supporting Information). The tumor volumes were then measured with an interval of 3 d. As shown in **Figure 4**a,b, a remarkable decrease in the tumor volume was observed from the third day in the Fe_5C_2-$Z_{HER2:342}$ with NIR group, and from the sixth day on, tumors were eliminated completely without relapse within 45 d. For the mouse group administrated with Fe_5C_2-PEG NPs, tumors were slightly inhibited in the preliminary 6 d, but recrudesced in the following days. No obvious tumor regression was observed in the Fe_5C_2-$Z_{HER2:342}$-only, laser-only, or control groups during the treatment. One mouse from each group was sacrificed on the fourth day post-treatment, and hematoxylin and eosin (H&E) staining was applied on the tumor. Apparent extensive necrosis appeared on mouse treated with PTT, which was mediated by Fe_5C_2-$Z_{HER2:342}$ NPs, while less necrotic areas were observed in the mouse subjected to PTT by Fe_5C_2-PEG NPs. No obvious malignant necrosis was exhibited in the other three groups (Figure 4c). MR images which were taken on the 45th day post-treatment demonstrated that tumors in the Fe_5C_2-$Z_{HER2:342}$ treated without laser group boomed dramatically, while for the mice under PTT by Fe_5C_2-$Z_{HER2:342}$, no tumor could be observed (Figure 4d). No mice died during the course of therapy. Moreover, no abnormality in body weight, eating, drinking, or other daily activity was observed (Figure 4e). Mice were then sacrificed at the 45th day for examination of any effects on major organs by investigating viscera index and H&E staining, which revealed no significant abnormality in major organs (Figure S15 and S16, Supporting Information). The results proposed that Fe_5C_2-$Z_{HER2:342}$ NPs might be an ideal candidate for targeted therapeutics by photothermal ablations.

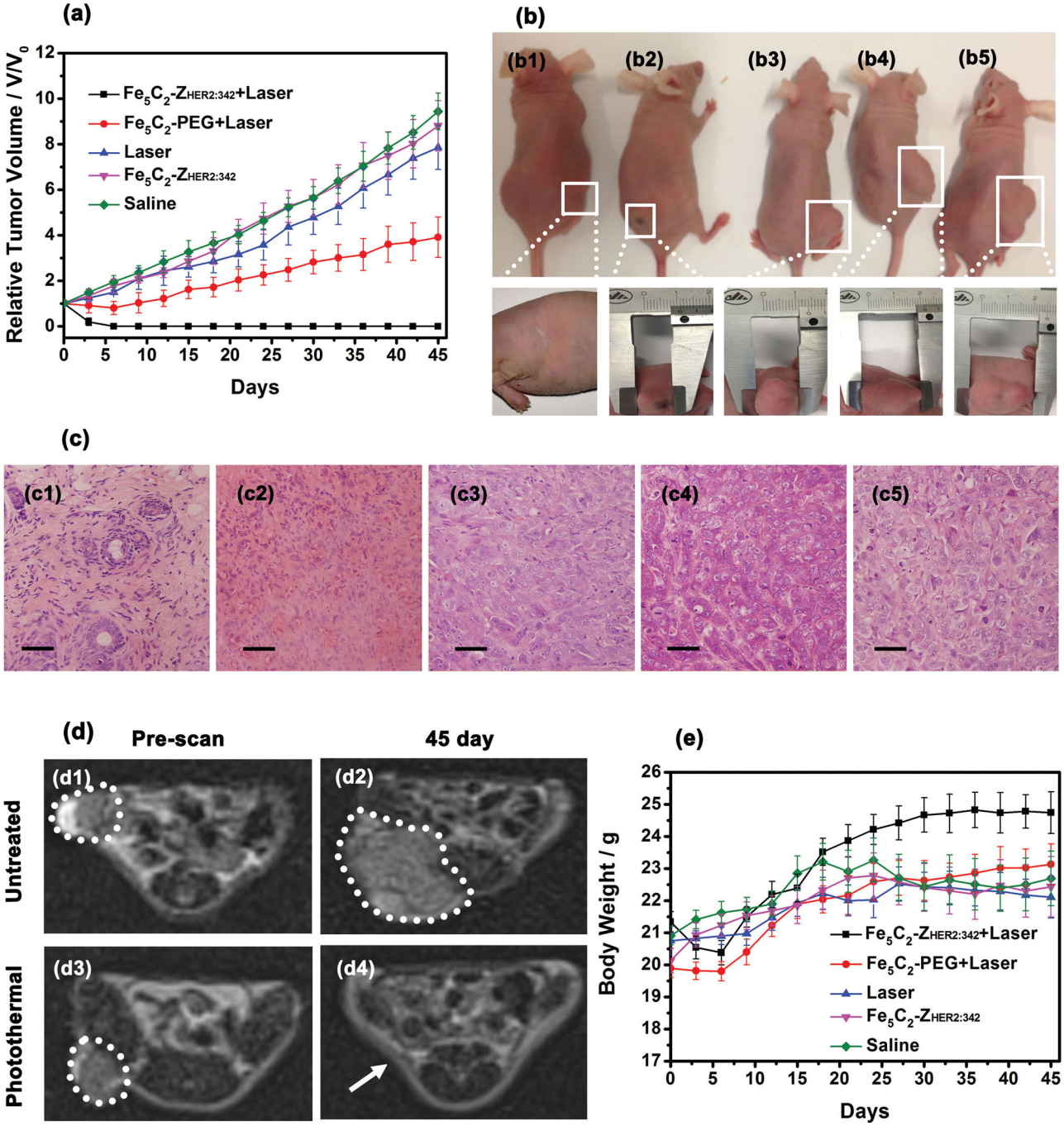

Figure 4. a) Tumor growth curves of different groups of tumor-bearing mice after treatment. The tumor sites are at the right rear flank, and the tumor volumes were normalized to their initial sizes. Error bars represent the standard deviations of 5 mice per group. b) Photographs at day 45 of representative mice from group: b1) Fe_5C_2-$Z_{HER2:342}$ with laser, b2) Fe_5C_2-PEG with laser, b3) laser only, b4) Fe_5C_2-$Z_{HER2:342}$ only, and, b5) control. The second row is the enlargements of the cited parts in the first row. c) H&E stained tumor sections collected from different groups of mice 4 days post treatment: c1) Fe_5C_2-$Z_{HER2:342}$ with laser; c2) Fe_5C_2-PEG with laser; c3) laser only; c4) Fe_5C_2-$Z_{HER2:342}$ only; and, c5) saline. Scale bars are 50 μm. d) T_2 MR images of mice: d1,d3) before, and, d2,d4) 45 d after treating; the (d2) mouse was injected with Fe_5C_2-$Z_{HER2:342}$ only, and the (d4) mouse was injected with Fe_5C_2-$Z_{HER2:342}$, and irradiated under 808 nm for 3 min at the tumor site 24 h after injection. e) Body weight of mice in different groups. The error bars represent the standard deviations (5 mice per group).

In summary, we have successfully designed Fe_5C_2 NPs as a probe with multifunctional feature for targeted tumor diagnosis and therapy. This new class of NPs reveals small sizes, high magnetization, satisfied stability, as well as high NIR absorbance and conversion. Benefiting from these fantastic properties, the Fe_5C_2-based probe exhibits high contrast in MRI, enhanced photoacoustic tomography and efficient photothermal therapy. By conjugating with the targeted affibody

Adv. Mater. 2014,
DOI: 10.1002/adma.201305811

$Z_{HER2:342}$, the Fe_5C_2-based probe can target tumor cells with low cytotoxicity, and selectively kill them through laser radiation. Moreover, the Fe_5C_2-$Z_{HER2:342}$ probe achieved in vivo efficient tumor ablation, excellent MRI, and photoacoustic tomography contrast effect. No noticeable side effects were observed from our injected dose. This work highlights the great potential of Fe_5C_2 NPs as multifunctional probes for imaging-guided cancer therapy.

Supporting Information

Supporting Information is available from the Wiley Online Library or from the author.

Acknowledgements

This work was supported in part by National Natural Science Foundation of China (NSFC) (nos. 51125001, 51172005, 90922033, 61078073, 81172182, and 21105120), the National Basic Research Program of China (no. 2010CB934601), the Research Fellowship for International Young Scientists of the National Natural Science Foundation of China (grant no. 51250110078), the Doctoral Program (no. 20090001120010), the Natural Science Foundation of Beijing (2122022), NSFC/RGC Joint Research Scheme (51361165201) and PKU COE-Health Science Center Seed Fund.

Received: November 25, 2013
Revised: February 22, 2014
Published online:

[1] R. Siegel, D. Naishadham, A. Jemal, *Ca-Cancer J. Clin.* **2013**, *63*, 11.
[2] a) W. S. Seo, J. H. Lee, X. Sun, Y. Suzuki, D. Mann, Z. Liu, M. Terashima, P. C. Yang, M. V. McConnell, D. G. Nishimura, H. Dai, *Nat. Mater.* **2006**, *5*, 971; b) H. Liu, D. Chen, L. Li, T. Liu, L. Tan, X. Wu, F. Tang, *Angew. Chem. Int. Ed.* **2011**, *50*, 891; c) C. Yue, P. Liu, M. Zheng, P. Zhao, Y. Wang, Y. Ma, L. Cai, *Biomaterials* **2013**, *34*, 6853.
[3] a) W. I. Choi, J.-Y. Kim, C. Kang, C. C. Byeon, Y. H. Kim, G. Tae, *ACS Nano* **2011**, *5*, 1995; b) H. Yuan, A. M. Fales, T. Vo-Dinh, *J. Am. Chem. Soc.* **2012**, *134*, 11358; c) Y. Wang, K. C. L. Black, H. Luehmann, W. Li, Y. Zhang, X. Cai, D. Wan, S.-Y. Liu, M. Li, P. Kim, Z.-Y. Li, L. V. Wang, Y. Liu, Y. Xia, *ACS Nano* **2013**, *7*, 2068; d) J. Chen, C. Glaus, R. Laforest, Q. Zhang, M. Yang, M. Gidding, M. J. Welch, Y. Xia, *Small* **2010**, *6*, 811; e) S.-M. Lee, H. J. Kim, Y.-J. Ha, Y. N. Park, S.-K. Lee, Y.-B. Park, K.-H. Yoo, *ACS Nano* **2012**, *7*, 50.
[4] a) Q. Tian, J. Hu, Y. Zhu, R. Zou, Z. Chen, S. Yang, R. Li, Q. Su, Y. Han, X. Liu, *J. Am. Chem. Soc.* **2013**, *135*, 8571; b) Y. S. Chen, W. Frey, S. Kim, K. Homan, P. Kruizinga, K. Sokolov, S. Emelianov, *Opt. Express* **2010**, *18*, 8867.
[5] a) Z. Sheng, L. Song, J. Zheng, D. Hu, M. He, M. Zheng, G. Gao, P. Gong, P. Zhang, Y. Ma, L. Cai, *Biomaterials* **2013**, *34*, 5236; b) M. Li, X. Yang, J. Ren, K. Qu, X. Qu, *Adv. Mater.* **2012**, *24*, 1722; c) A. L. Antaris, J. T. Robinson, O. K. Yaghi, G. Hong, S. Diao, R. Luong, H. Dai, *ACS Nano* **2013**, *7*, 3644; d) S. Sherlock, H. Dai, *Nano Res.* **2011**, *4*, 1248.
[6] a) X. Liu, W.-C. Law, M. Jeon, X. Wang, M. Liu, C. Kim, P. N. Prasad, M. T. Swihart, *Adv. Healthcare Mater.* **2013**, *2*, 952; b) S. Wang, P. Huang, L. Nie, R. Xing, D. Liu, Z. Wang, J. Lin, S. Chen, G. Niu, G. Lu, X. Chen, *Adv. Mater.* **2013**, *25*, 3055.
[7] a) L.-S. Bouchard, M. S. Anwar, G. L. Liu, B. Hann, Z. H. Xie, J. W. Gray, X. Wang, A. Pines, F. F. Chen, *Proc. Natl. Acad. Sci. USA* **2009**, *106*, 4085; b) J.-S. Choi, J.-H. Lee, T.-H. Shin, H.-T. Song, E. Y. Kim, J. Cheon, *J. Am. Chem. Soc.* **2010**, *132*, 11015.
[8] a) D.-E. Lee, H. Koo, I.-C. Sun, J. H. Ryu, K. Kim, I. C. Kwon, *Chem. Soc. Rev.* **2012**, *41*, 2656; b) Y. Jin, C. Jia, S.-W. Huang, M. O'Donnell, X. Gao, *Nat. Commun.* **2010**, *1*, 41; c) W. Dong, Y. Li, D. Niu, Z. Ma, J. Gu, Y. Chen, W. Zhao, X. Liu, C. Liu, J. Shi, *Adv. Mater.* **2011**, *23*, 5392; d) X. Shi, H. Gong, Y. Li, C. Wang, L. Cheng, Z. Liu, *Biomaterials* **2013**, *34*, 4786.
[9] a) Y. I. Park, H. M. Kim, J. H. Kim, K. C. Moon, B. Yoo, K. T. Lee, N. Lee, Y. Choi, W. Park, D. Ling, K. Na, W. K. Moon, S. H. Choi, H. S. Park, S.-Y. Yoon, Y. D. Suh, S. H. Lee, T. Hyeon, *Adv. Mater.* **2012**, *24*, 5755; b) S. Wang, P. Huang, L. Nie, R. Xing, D. Liu, Z. Wang, J. Lin, S. Chen, G. Niu, G. Lu, X. Chen, *Adv. Mater.* **2013**, *25*, 3055; c) J. Kim, Y. Piao, T. Hyeon, *Chem. Soc. Rev.* **2009**, *38*, 372.
[10] a) N. Lee, Y. Choi, Y. Lee, M. Park, W. K. Moon, S. H. Choi, T. Hyeon, *Nano Lett.* **2012**; b) S. Mathur, L. Xiao, J. Li, D. F. Brougham, E. K. Fox, N. Feliu, A. Bushmelev, A. Schmidt, N. Mertens, F. Kiessling, M. Valldor, B. Fadeel, *ACS Nano* **2011**, *5*, 6315.
[11] a) K. Yang, L. Hu, X. Ma, S. Ye, L. Cheng, X. Shi, C. Li, Y. Li, Z. Liu, *Adv. Mater.* **2012**, *24*, 1868; b) H.-W. Yang, H.-L. Liu, M.-L. Li, I. W. Hsi, C.-T. Fan, C.-Y. Huang, Y.-J. Lu, M.-Y. Hua, H.-Y. Chou, J.-W. Liaw, C.-C. M. Ma, K.-C. Wei, *Biomaterials* **2013**, *34*, 5651.
[12] C. Yang, H. Zhao, Y. Hou, D. Ma, *J. Am. Chem. Soc.* **2012**, *134*, 15814.
[13] A. Orlova, M. Magnusson, T. L. J. Eriksson, M. Nilsson, B. Larsson, I. Hoiden-Guthenherg, C. Widstrom, J. Carlsson, V. Tolmachev, S. Stahl, F. Y. Nilsson, *Cancer Res.* **2006**, *66*, 4339.
[14] S. Sun, H. Zeng, D. B. Robinson, S. Raoux, P. M. Rice, S. X. Wang, G. Li, *J. Am. Chem. Soc.* **2003**, *126*, 273.
[15] S. Laurent, D. Forge, M. Port, A. Roch, C. Robic, L. Vander Elst, R. N. Muller, *Chem. Rev.* **2008**, *108*, 2064.
[16] J.-t. Jang, H. Nah, J.-H. Lee, S. H. Moon, M. G. Kim, J. Cheon, *Angew. Chem. Int. Ed.* **2009**, *48*, 1234.
[17] B. Nikoobakht, M. A. El-Sayed, *Chem. Mater.* **2003**, *15*, 1957.
[18] S. Q. Ye, J. Y. Yang, J. Z. Xi, Q. S. Ren, C. H. Li, *Chin. Opt. Lett.* **2012**, *10*, 121701.
[19] a) A. Cirstoiu-Hapca, L. Bossy-Nobs, F. Buchegger, R. Gurny, F. Delie, *Int. J. Pharm.* **2007**, *331*, 190; b) Y. M. Xu, L. F. Wang, L. T. Jia, X. C. Qiu, J. Zhao, C. J. Yu, R. Zhang, F. Zhu, C. J. Wang, B. Q. Jin, S. Y. Chen, A. G. Yang, *J. Immunol.* **2004**, *173*, 61; c) B. W. Park, K. S. Kim, M. K. Heo, K. S. Lee, E. K. Kim, *Yonsei Med. J.* **2003**, *44*, 58.